THE ASTROPHYSICAL JOURNAL, 489:37–48, 1997 November 1

REDSHIFT-SPACE DISTORTIONS AND THE REAL-SPACE CLUSTERING OF DIFFERENT GALAXY TYPES

LUIGI GUZZO,[1,2] MICHAEL A. STRAUSS,[1,3] KARL B. FISHER,[4,5] RICCARDO GIOVANELLI,[6] AND MARTHA P. HAYNES[6]

Received 1997 April 28; accepted 1997 June 12

ABSTRACT

We study the distortions induced by peculiar velocities on the redshift-space correlation function of galaxies of different morphological types in the Pisces-Perseus redshift survey. Redshift-space distortions affect early- and late-type galaxies in different ways. In particular, at small separations the dominant effect comes from virialized cluster cores, where ellipticals are the dominant population. The net result is that a meaningful comparison of the clustering strength of different morphological types can be performed only in real space, i.e., after projecting out the redshift distortions on the two-point correlation function $\xi(r_p, \pi)$. A power-law fit to the projected function $w_p(r_p)$ on scales smaller than 10 h^{-1} Mpc gives $r_0 = 8.35^{+0.75}_{-0.76}$ h^{-1} Mpc, $\gamma = 2.05^{+0.10}_{-0.08}$ for the early-type population, and $r_0 = 5.55^{+0.40}_{-0.45}$ h^{-1} Mpc, $\gamma = 1.73^{+0.07}_{-0.08}$ for spirals and irregulars. These values are derived for a sample luminosity limited to $M_{Zw} \leq -19.5$. We detect a 25% increase of r_0 with luminosity for all types combined, from $M_{Zw} = -19$ to -20. In the framework of a simple stable clustering model for the mean streaming of pairs, we estimate $\sigma_{12}(1)$, the one-dimensional pairwise velocity dispersion between 0 and 1 h^{-1} Mpc, to be 865^{+250}_{-165} km s^{-1} for early-type galaxies and 345^{+95}_{-65} km s^{-1} for late types. This latter value should be a fair estimate of the pairwise dispersion for "field" galaxies; it is stable with respect to the presence or absence of clusters in the sample, and is consistent with the values found for noncluster galaxies and *IRAS* galaxies at similar separations.

Subject headings: galaxies: clusters: general — galaxies: distances and redshifts — galaxies: structure

1. INTRODUCTION

Peculiar velocities distort maps of galaxy distribution when redshifts are used as a measure of distance through the Hubble relation. The observed distortions contain important information about the statistical properties of the large-scale motions of galaxies, presumably due to the gravitational influence of the true underlying mass distribution. In particular, the two-point correlation function in redshift space, $\xi(s)$, differs from that in real space, $\xi(r)$, in two respects. On small scales correlations are suppressed due to the virialized motions in rich clusters, which in redshift space elongate structures along the line of sight, while on large scales coherent motions produced by infall into overdense regions or by outflow out of underdense regions enhance correlations.

Galaxies of different morphological types inhabit different environments, following a well-established morphology-density relation (e.g., Dressler 1980; Postman & Geller 1984). As a consequence, they display significantly different clustering properties (Davis & Geller 1976; Giovanelli, Haynes, & Chincarini 1986; Iovino et al. 1993; Loveday et al. 1995; Hermit et al. 1996); ellipticals and S0's dominate dense cluster cores and are therefore more clustered than spirals and irregulars. However, their association with the deep potential wells of clusters implies that they have higher peculiar velocities on average, so that the small-scale $\xi(s)$ for early-type galaxies is more strongly suppressed with respect to $\xi(r)$ than for late types. The consequence is that a correct comparison of the clustering properties of different morphological types requires a detailed understanding of their respective redshift-space distortions. One way to avoid this problem is to measure the angular correlation function $w(\theta)$ on two-dimensional catalogues (Giovanelli et al. 1986; Loveday et al. 1995).[7] The effects of redshift-space distortions must also be quantified in comparing the angular clustering of distant objects with the clustering in redshift space of galaxies at low redshift (e.g., Iovino et al. 1996).

The standard method for quantifying redshift distortions is to split the separation vector of a pair of objects into components lying on the plane of the sky, r_p, and along the line of sight, π, and to compute the correlation function $\xi(r_p, \pi)$ as a function of these two components. The iso-correlation contours of $\xi(r_p, \pi)$ will be stretched along the π direction at small separations, because of the effect of large velocity dispersions, and compressed at large scales as a consequence of large-scale coherent motions. Projecting $\xi(r_p, \pi)$ onto the r_p axis gives the projected function $w_p(r_p)$, which is independent of redshift distortions and can be directly expressed as an integral over the real-space correlation function $\xi(r)$. The equation relating $w_p(r_p)$ and $\xi(r)$ thus allows one to recover the latter via direct inversion or modeling.

On the other hand, modeling the distortions of $\xi(r_p, \pi)$ allows one to characterize the pairwise velocity distribution function. In this paper, we are particularly concerned with the second moment of this distribution function, $\sigma_{12}(r)$.

[1] Department of Astrophysical Sciences, Princeton University, Princeton, NJ 08544.

[2] Permanent Address: Osservatorio Astronomico di Brera, Via Bianchi 46, I–22055 Merate (LC), Italy.

[3] Alfred P. Sloan Foundation Fellow.

[4] Institute for Advanced Study, Olden Lane, Princeton, NJ 08540.

[5] Current Address: Signal Physics Group, Applied Research Laboratories, University of Texas, Austin, TX 78713.

[6] Department of Astronomy and Center for Radiophysics and Space Research, Space Sciences Building, Cornell University, Ithaca, NY 14853.

[7] These latter authors also perform a cross correlation between morphological subsamples of the APM-Stromlo redshift survey and the APM angular catalogue; see § 4.2.

Davis & Peebles (1983, hereafter DP83) used the CfA1 survey (Huchra et al. 1983) to measure $\sigma_{12}(1)$, the value of $\sigma_{12}(r)$ at $r = 1\ h^{-1}$ Mpc, to be 340 ± 40 km s^{-1}. While the analysis of the *IRAS* 1.2 Jy redshift survey by Fisher et al. (1994b, hereafter F94b) produced a similar result ($\sigma_{12}(1) = 317^{+40}_{-49}$ km s^{-1}), reanalyses of the CfA1 survey (Mo, Jing, & Börner 1993; Zurek et al. 1994; Somerville, Davis, & Primack 1996) and of larger optical-redshift surveys have shown a large range of values, up to 1000 km s^{-1} (Marzke et al. 1995; Guzzo et al. 1996; Lin 1995). In particular, $\sigma_{12}(1)$ is found to be quite sensitive to the presence or absence of one or two rich clusters, even in volumes as large as in CfA2. It seems plausible that while the CfA1 value was strongly affected by the smallness of the volume surveyed, that of the *IRAS* 1.2 Jy survey reflects the specific nature of *IRAS* galaxies, mostly star-forming, late-type galaxies that are underrepresented in rich clusters relative to optically selected galaxies (Strauss et al. 1992).

The case of the *IRAS* galaxies explicitly illustrates the dangers of using a specific class of objects to draw conclusions about statistics of the velocity field, in particular at small separations, as the answers depend sensitively on the morphological type of the tracer used. This paper addresses this issue in detail, asking 1) What is the difference in the clustering strength of early- and late-type galaxies measured in real space? and 2) What is the small-scale velocity dispersion for the two classes of objects? In § 2, we present the data used for our analyses. We discuss the measurement of $\xi(r_p, \pi)$ in § 3, and present our results in § 4. Our conclusions are summarized in § 5.

2. THE DATA: DEFINITION OF THE SAMPLES

We use the Perseus-Pisces redshift catalogue (cf. Giovanelli & Haynes 1991), which includes redshifts for all Zwicky galaxies (Zwicky et al. 1961–1968) in the positive-declination area of the south Galactic cap (i.e., about $21^h \leq \alpha \leq 5^h$, $0° \leq \delta \leq 50°$). As Giovanelli et al. (1986) make clear, the Perseus-Pisces redshift survey is affected by Galactic extinction around the edges. For statistical studies, therefore, it must be properly restricted. The Zwicky catalogue is nominally complete to $m_{Zw} = 15.7$; we thus impose an extinction-corrected magnitude cut of 15.5, trim the survey to $22^h \leq \alpha \leq 4^h$, $0° \leq \delta \leq 42°$, and apply the additional cut indicated by the heavy line in Figure 1. This excludes nearly all regions with absorption $A_B > 0.2$, as given by the extinction maps of Burstein & Heiles (1978), while it leaves the core of the Perseus cluster ($\alpha \sim 3^h.2$, $\delta \sim +41°$) to allow us to study the robustness of our results to the presence of the richest cluster in the region. The magnitude-limited sample selected in this way contains 4111 galaxies. One potential problem of our selection criteria is that they push the Zwicky catalogue to its completeness limit. In particular, with the extinction correction, we include galaxies with observed Zwicky magnitudes $m_{Zw} \gtrsim 15.5$, where magnitude errors are large (e.g., Bothun & Cornell 1990). We shall show in § 4.2 that our principal results are indeed quite robust to these uncertainties in the parent photometric catalogue.

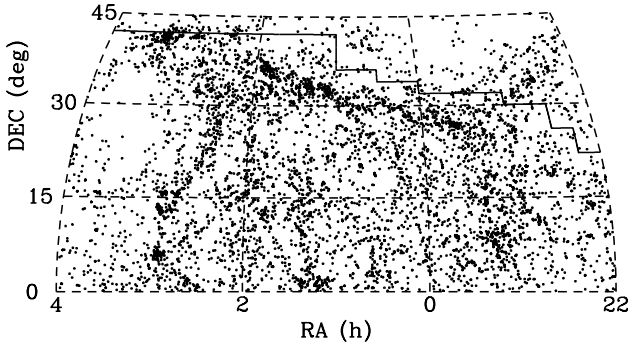

FIG. 1.—The distribution on the sky of all galaxies with $M_{Zw} \leq 15.5$, after correction for extinction. The upper solid line marks the border of the high-extinction region excluded from the sample. The large lump of objects near $\alpha \sim 3^h.2$, $\delta \sim 41°$ is the Perseus cluster.

All the analyses in this paper are done with volume-limited subsamples of the data. That is, we select a lower-limit luminosity (or equivalently, an upper limit in absolute magnitude), and a corresponding maximum distance implied by our apparent magnitude limit, giving us uniform sampling throughout the volume. This has the effect of de-emphasizing the Pisces-Perseus chain relative to the magnitude-limited case, because in the latter the selection function peaks near the redshift of the supercluster This choice is also crucial for discussing luminosity effects, and eliminates uncertainties related to the weighting schemes necessary when analyzing magnitude-limited samples.

Table 1 summarizes the parameters of the volume-limited samples we have used. The range of absolute magnitudes covered by the subsamples reflects the need to maximize our volume while keeping a sufficient number of objects within it. Absolute magnitudes were calculated assuming $H_0 = 100$ km s^{-1} Mpc^{-1}. The E-19.5 sample ("ellipticals") contains galaxies with early morphological types (E, S0, and S0a), while the S samples ("spirals") contain all galaxies classified as spirals or irregulars. The morphological information available in the catalogue is in reality quite finer, subdivided into 14 classes. The morphological coding is from the UGC for galaxies in that catalog, and has been estimated from sky survey plates for the remainder of the galaxies (Giovanelli et al. 1986). To maximize the statistics within the volume-limited samples, we restrict our analysis to the two broad groups of early- and late-type galaxies. The spiral class is, however, large enough to define several samples to different absolute magnitudes (S-19, S-19.5, and S-20); we also define a spiral sample trimmed to exclude the Perseus cluster (S-19.5 [NP]). Finally, we define an equivalent sample including all morphologies for comparison, PP-19.5 (NP).

The cone diagrams of Figure 2 show the galaxy distribution in PP-19.5 and PP-20, in which all morphological types are included, while Figure 3 shows the corresponding distribution for the E-19.5 and S-19.5 samples, respectively.

TABLE 1

PROPERTIES OF THE VOLUME-LIMITED SUBSAMPLES

Sample	M_{lim}	d_{lim} (h^{-1} Mpc)	Morphology	N_{gal}
PP-19	−19	79	All	1021
PP-19.5	−19.5	100	All	852
PP-19.5 (NP)	−19.5	100 (No Perseus)	All	803
PP-20	−20	126	All	577
S-19	−19	79	Late	565
S-19.5	−19.5	100	Late	481
S-19.5 (NP)	−19.5	100 (No Perseus)	Late	458
S-20	−20	126	Late	333
E-19.5	−19.5	100	Early	278

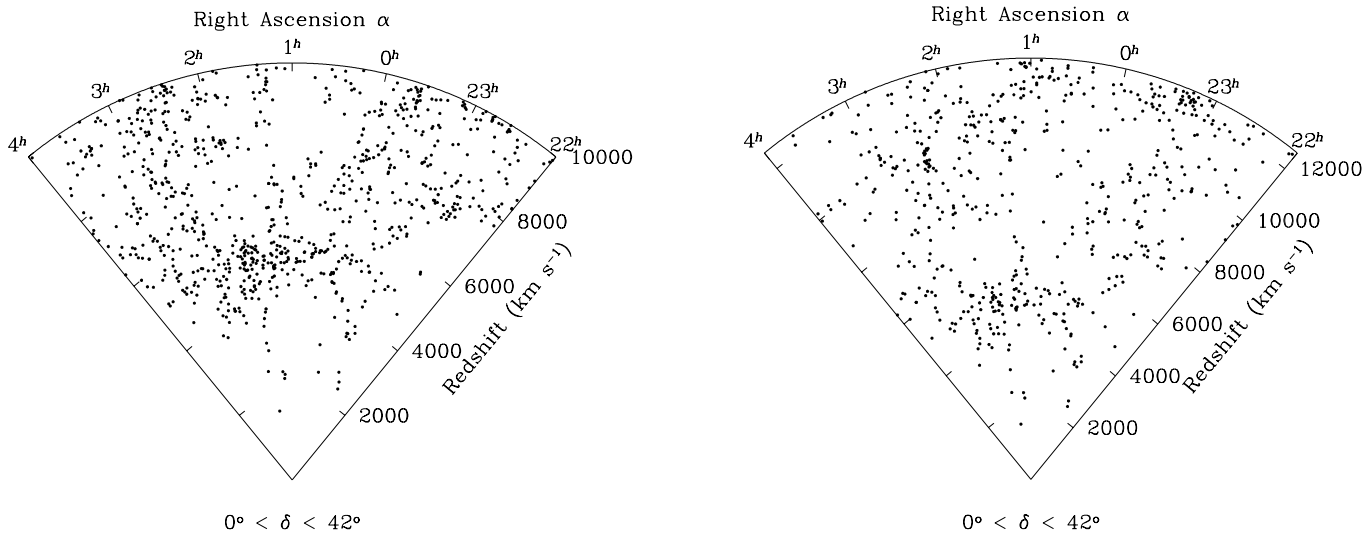

FIG. 2.—Galaxy distribution in the volume-limited samples to $M_{Zw} = -19.5$ and $M_{Zw} = -20$, including all morphological types

Note that the Perseus-Pisces chain, the overdensity at $cz \approx 6000$ km s^{-1}, is more prominent in the ellipticals than the spirals, consistent with the observed distribution on the sky (Giovanelli et al. 1986). This is made quantitative in Figure 4, which shows the redshift histogram of each of these subsamples; the dashed line in each case, proportional to r^2, gives the expected distribution in the absence of structure.

3. ESTIMATING THE TWO-POINT CORRELATION FUNCTION IN REDSHIFT SPACE

3.1. *Definitions of r_p and π*

The effect of redshift-space distortions can be understood through the correlation function $\xi(r_p, \pi)$, where the radial separation of pairs is split into two components: π, parallel to the line of sight, and r_p, perpendicular to it. There are two definitions of these quantities in the literature. Given two galaxies at redshifts v_1 and v_2 separated by angle θ, DP83 define

$$\pi \equiv \frac{1}{H_0} |v_1 - v_2| , \quad r_p \equiv \frac{1}{H_0} (v_1 + v_2) \tan\left(\frac{\theta}{2}\right) . \quad (1)$$

Note that the quadrature sum of r_p and π is *not* equal to the redshift-space distance s between the galaxies. Recognizing this, Fisher et al. (1994a, hereafter F94a) use a slightly different definition. They define the line-of-sight vector $\boldsymbol{l} \equiv (\boldsymbol{v}_1 + \boldsymbol{v}_2)/2$ and the redshift difference vector $\boldsymbol{s} \equiv \boldsymbol{v}_1 - \boldsymbol{v}_2$, leading to the definitions

$$\pi \equiv \frac{\boldsymbol{s} \cdot \boldsymbol{l}}{H_0 |\boldsymbol{l}|} , \quad r_p^2 \equiv \frac{\boldsymbol{s} \cdot \boldsymbol{s}}{H_0^2} - \pi^2 . \quad (2)$$

If we recast the F94a formulation in terms of θ, we find

$$\pi = \frac{1}{H_0} |v_1 - v_2| + \mathcal{O}(\theta^2) ,$$

$$r_p \simeq \frac{1}{H_0} (v_1 + v_2) \tan\left(\frac{\theta}{2}\right) \frac{4 v_1 v_2}{(v_1 + v_2)^2} , \quad (3)$$

which shows explicitly that the two definitions are *not* strictly equivalent, even in the small-angle approximation. For our analysis we use equation (2), but checks using equation (1) show only negligible differences in our $\xi(r_p, \pi)$ maps. We conclude therefore that one can make direct com-

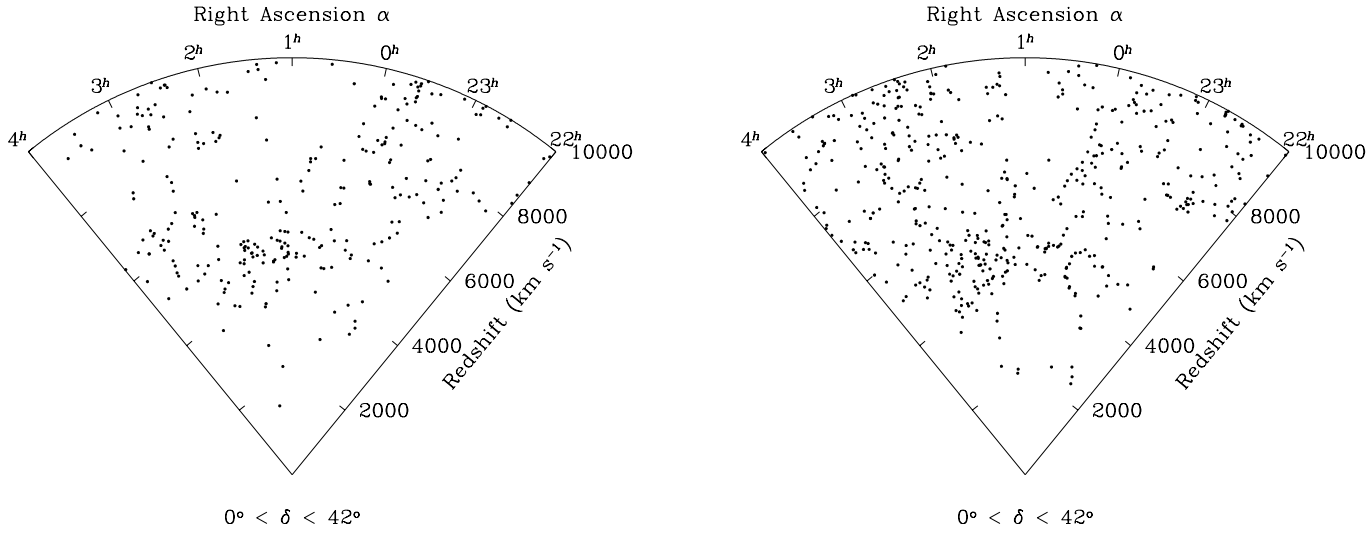

FIG. 3.—Spatial distribution of early- and late-type galaxies, volume-limited to $M_{Zw} = -19.5$

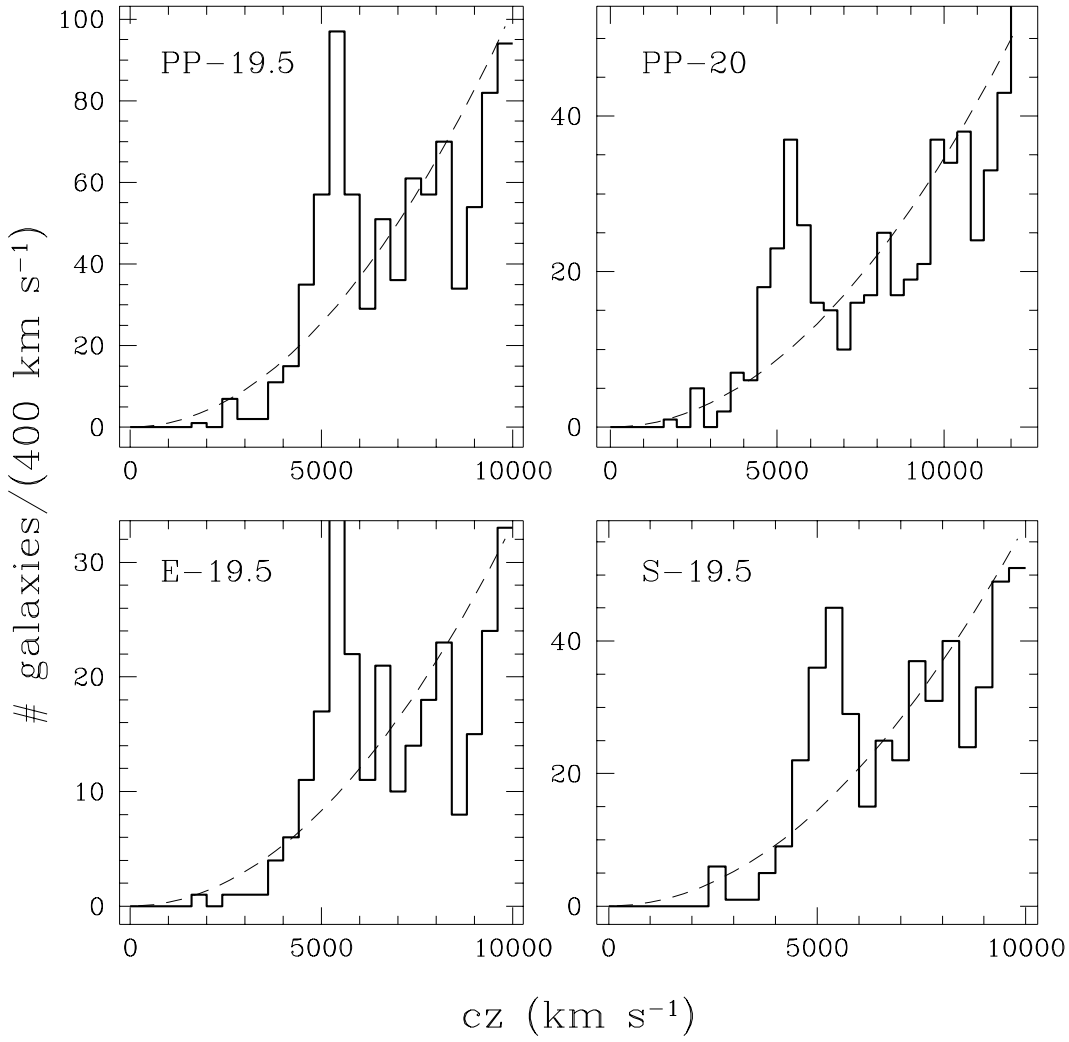

FIG. 4.—Histograms of the redshift distribution in four representative volume-limited samples. *Top panels*: all galaxies. *Bottom panels*: early-type and late-type galaxies separately. Dashed lines are the distributions expected in the absence of structure.

parison of results obtained with the two different definitions.

3.2. *Measuring* $\xi(r_p, \pi)$

We estimate the quantity $\xi(r_p, \pi)$ using the method of DP83. A catalog of $n_R = 100{,}000$ uniformly distributed points with the same boundaries as the real sample is prepared. We count the number of pairs in 1 h^{-1} Mpc bins of r_p and π among the n_G galaxies $[N_{GG}(r_p, \pi)]$ and between the galaxies and the random sample $[N_{GR}(r_p, \pi)]$. Our estimate of the correlation function is then

$$\xi(r_p, \pi) = \frac{N_{GG}(r_p, \pi)}{N_{GR}(r_p, \pi)} \frac{2n_R}{n_G} - 1 \, . \tag{4}$$

Because our samples are volume-limited, each galaxy gets equal weight, and thus we do not apply the statistical weights needed when analyzing magnitude-limited catalogues. For the most part we confine ourselves to scales less than 10 h^{-1} Mpc, so there is little benefit to using the alternative estimator of Hamilton (1993). This is less sensitive than equation (4) to uncertainties in the mean density, and is therefore chiefly important when measuring the correlation function on very large scales.

3.3. *Error Estimation and Maximum-likelihood Fits*

Following Ling, Frenk, & Barrow (1986), we use bootstrap resampling to compute statistical errors in our estimates of quantities derived from $\xi(r_p, \pi)$. As seen in the next section, we carry out quantitative analyses not on $\xi(r_p, \pi)$ directly, but rather on two derived quantities: w_p (eq. [5]), the projection of $\xi(r_p, \pi)$ on the r_p axis, which does not suffer redshift-space distortions, and $\bar{\xi}(\pi)$ (eq. [11]), essentially a cut made in $\xi(r_p, \pi)$ at constant r_p in order to measure redshift-space distortions. We thus compute errors and the covariance matrix for the one-dimensional quantities w_p and $\bar{\xi}(\pi)$ rather than for the two-dimensional $\xi(r_p, \pi)$. For each of the samples listed in Table 1, we create 100 bootstrap realizations and compute w_p and $\bar{\xi}(\pi)$ for each. Determination of the covariance matrix of errors is then straightforward, following F94a. F94a have discussed the method in detail, showing that it gives a good representation of true statistical errors for the correlation function on scales below $\sim 10\, h^{-1}$ Mpc, but tends to overestimate them on larger scales.

This covariance matrix enables us to fit models for the real-space correlation function $\xi(r)$ and the redshift distortions to the observed w_p and $\bar{\xi}(\pi)$ via χ^2 (see F94b). In

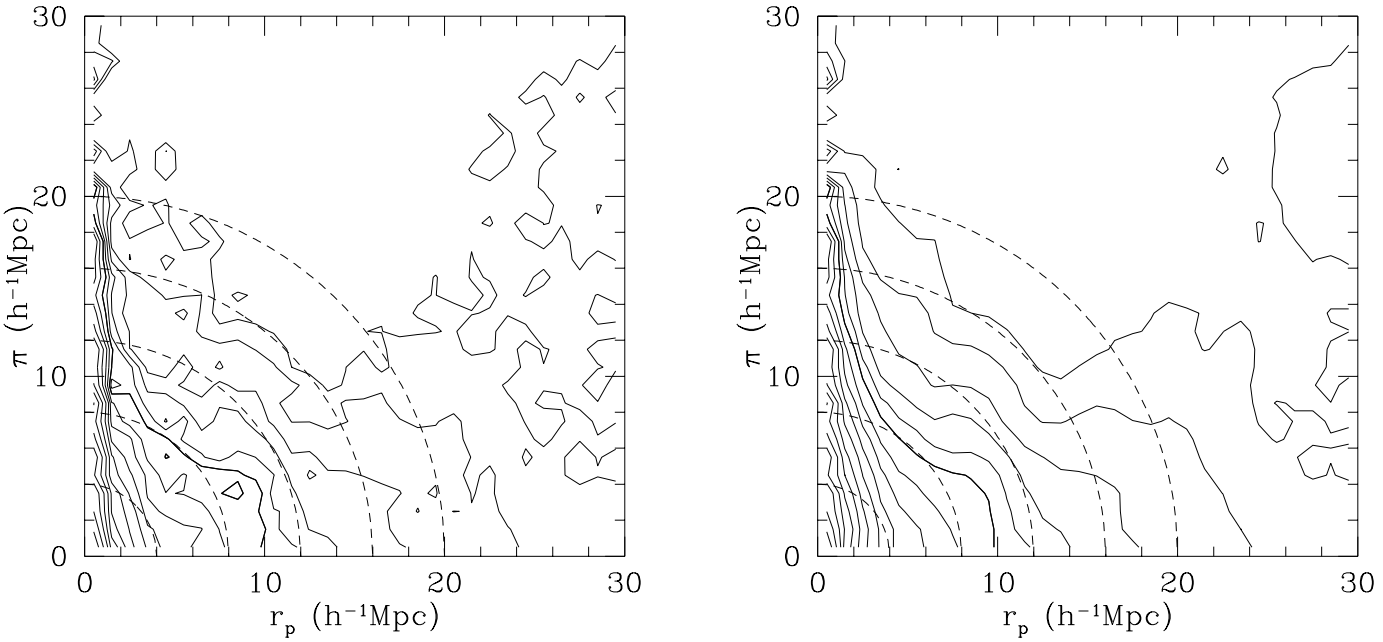

FIG. 5.—$\xi(r_p, \pi)$ for PP-19. In this and the following $\xi(r_p, \pi)$ maps, the heavy contour corresponds to $\xi = 1$; for larger values of ξ, contours are logarithmically spaced, with $\Delta \log_{10} \xi = 0.1$; below $\xi = 1$ they are linearly spaced, with $\Delta\xi = 0.2$ down to $\xi = 0$. Dashed contours represent the isotropic correlations expected in the absence of peculiar velocities. The right-hand panel has been Gaussian-smoothed with an isotropic filter of width $3\ h^{-1}$ Mpc.

practice, the effective number of degrees of freedom in the data is smaller than the number of sampled values of w_p and $\xi(\pi)$ (i.e., these functions are oversampled), and thus the covariance matrix is singular. We therefore follow F94b in using singular value decomposition, which allows the calculation of the matrix product in the χ^2 function in a robust manner.

4. REDSHIFT-SPACE DISTORTIONS: $\xi(r_p, \pi)$

4.1. *The Observed* $\xi(r_p, \pi)$

Figures 5, 6, and 7 display the observed $\xi(r_p, \pi)$ for the complete samples PP-19, PP-19.5, and PP-20, and for the morphological subsamples E-19.5 and S-19.5. For PP-19 we show the original $\xi(r_p, \pi)$, while for all samples we show a version smoothed by a $3\ h^{-1}$ Mpc $\times$ $3\ h^{-1}$ Mpc Gaussian to suppress the binning noise and to bring out the global features of the maps. All of the statistical analyses below are of course carried out on the unfiltered data.

The contours for PP-19 and PP-19.5 are enormously distorted at very small scales, a signature of a high pairwise dispersion $\sigma_{12}(r)$ at small r, as we shall quantify in § 4.3. Most of this distortion is produced by pairs lying in clusters, in particular in the smallest sample, PP-19, which is dominated by a half-dozen rich clusters along the Perseus-Pisces chain. The small-scale elongations are substantially smaller

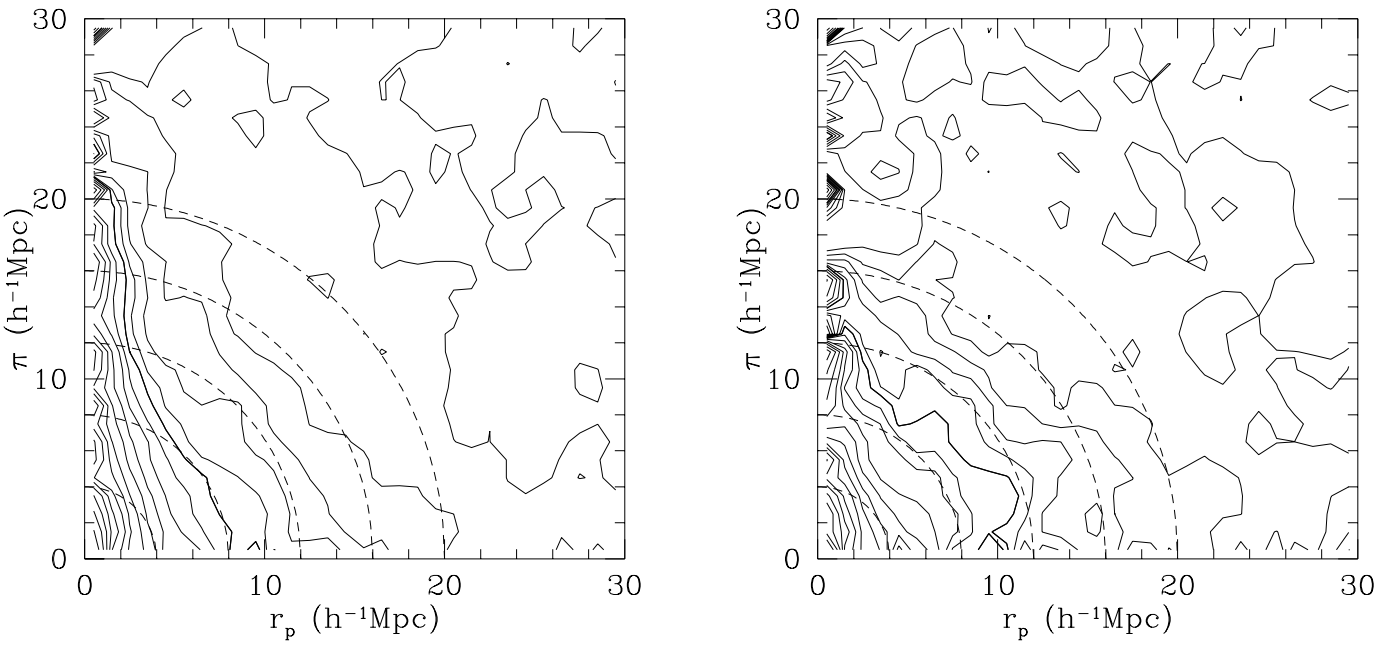

FIG. 6.—$\xi(r_p, \pi)$ for PP-19.5 and PP-20, Gaussian smoothed

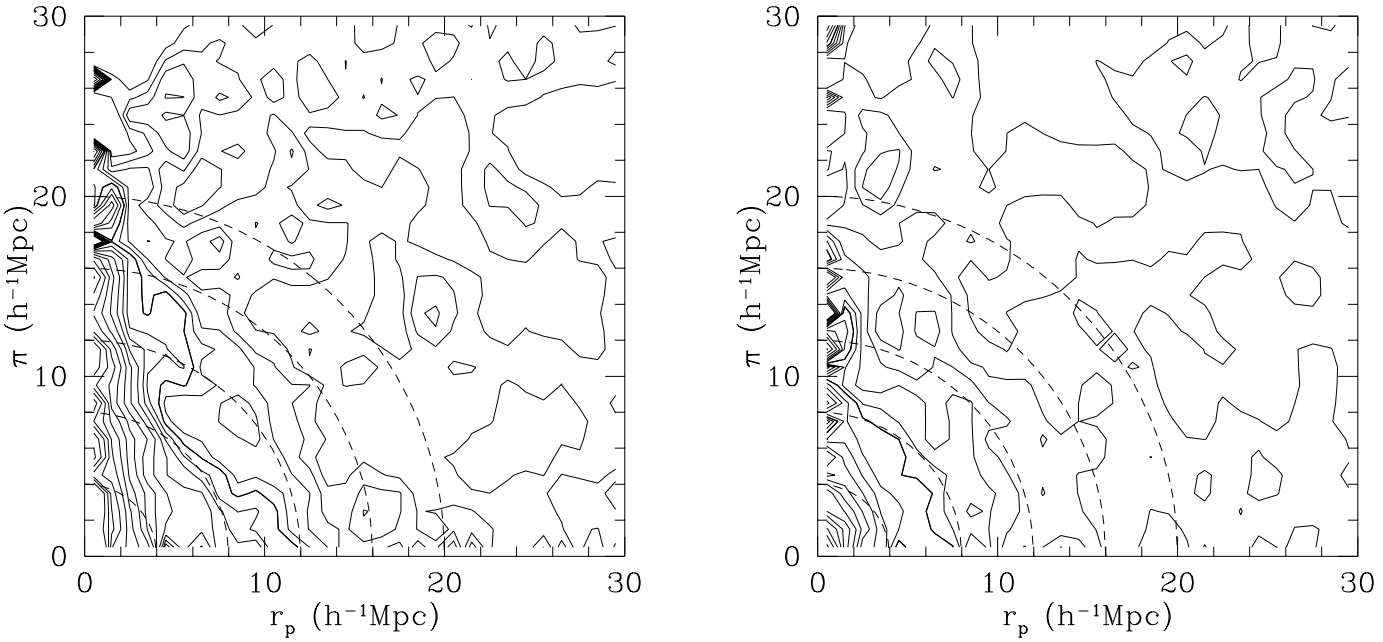

FIG. 7.—$\xi(r_p, \pi)$ for the early- and late-type samples E-19.5 and S-19.5, respectively, Gaussian-smoothed

in the PP-20 sample. This sample has a volume of 7.4×10^5 h^{-3} Mpc^3, quite a bit larger than PP-19.5, but it does not include more clusters, and therefore the cluster contribution to $\sigma_{12}(1)$ is somewhat diluted. This volume is still a factor of 6 smaller than the volume at which Marzke et al. (1995) showed that $\sigma_{12}(1)$ stabilizes, using both a *COBE*-normalized cold dark matter model and a phenomenological model based on the observed distribution of Abell cluster velocity dispersions. For sample volumes comparable to those used here, they derive a typical uncertainty for $\sigma_{12}(1)$ of ~ 180 km s^{-1}. Although this scatter refers to nonoverlapping samples, it does give an explanation for the observed difference in σ for PP-19 and PP-20.

On large scales, the compression of $\xi(r_p, \pi)$ for PP-19 [in particular the $\xi(r_p, \pi) = 0.2$ and $\xi(r_p, \pi) = 0$ contours] is as expected from large-scale streaming (see F94b). However, the Perseus-Pisces supercluster (see Fig. 2) lies largely in the plane of the sky, so the real-space distribution of galaxies is intrinsically anisotropic in this sample. Thus, it is not a fair sample for measuring large-scale streaming. Some part of the observed distortions of the $\xi(r_p, \pi)$ contours must be due to infall onto the supercluster itself, as directly observed by Giovanelli et al. (1996), who showed that galaxies out to 20 h^{-1} Mpc from the ridge display infall velocities of the order of 1000 km s^{-1} (see also Willick 1990; Eisenstein, Loeb, & Turner 1997). Unfortunately, there is no way to disentangle the two effects from $\xi(r_p, \pi)$ alone, and we will not discuss the large-scale distortions further in this paper.

Figure 7 shows $\xi(r_p, \pi)$ for E-19.5 and S-19.5. The visual difference between the two maps is impressive; the ellipticals display a huge small-scale elongation of the contours, while $\xi(r_p, \pi)$ for the spirals is much more isotropic. This figure demonstrates directly how different the dynamical behaviors of the two populations are, and how their real-space correlation functions are mapped into redshift space in very different ways.

We now proceed to quantify the real-space correlation function and redshift distortions from the observed $\xi(r_p, \pi)$.

4.2. *The Real-Space Correlation Function*

We project $\xi(r_p, \pi)$ onto the r_p axis by integrating over the dimension on which the redshift-space distortion acts, giving a quantity that is independent of the form and amount of the distortion itself,

$$w_p(r_p) \equiv 2 \int_0^\infty dy\ \xi(r_p, \pi) = 2 \int_0^\infty dy\ \xi[(r_p^2 + y^2)^{1/2}]\ , \quad (5)$$

in which the second equality follows from the independence of the integral from the redshift-space distortions. In the right-hand side of the expression, ξ is the real-space correlation function evaluated at $r = (r_p^2 + y^2)^{1/2}$. Modeling $\xi(r)$ as a power law, $\xi(r) = (r/r_0)^{-\gamma}$, allows us to carry out the integral analytically, yielding

$$w_p(r_p) = r_p \left(\frac{r_0}{r_p}\right)^\gamma \left[\Gamma\left(\frac{1}{2}\right)\Gamma\left(\frac{\gamma - 1}{2}\right) \Big/ \Gamma\left(\frac{\gamma}{2}\right)\right], \quad (6)$$

where Γ is the Gamma function. We choose $\pi_{\rm up}$, the upper integration limit in equation (5), to be large enough to give a stable estimate of w_p. For the PP-19 sample, $w_p(r_p)$ is quite insensitive to $\pi_{\rm up}$ in the range $20\ h^{-1}$ Mpc $< \pi_{\rm up} < 30$ h^{-1} Mpc for $r_p < 10\ h^{-1}$ Mpc. For larger values of r_p, $w_p(r_p)$ is fairly sensitive to $\pi_{\rm up}$, but since we are primarily interested in the redshift distortions on small scales this has no effect on our result.

The observed $w_p(r_p)$ and the best-fit power law for the complete samples are shown in Figure 8, together with likelihood contours on r_0 and γ, while the results of the fits are reported in Table 2. Note how well the power-law model fits the data[8]. Error bars are given by the scatter over 100 bootstrap realizations, and the fit is performed as discussed in § 3.3. There is evidence that the correlation length grows with increasing sample depth and intrinsic luminosity. This

[8] Note also, however, that $w_p(r_p)$ is an integral over $\xi(r)$, and that therefore small deviations from the power-law model in the latter function are averaged out in the former.

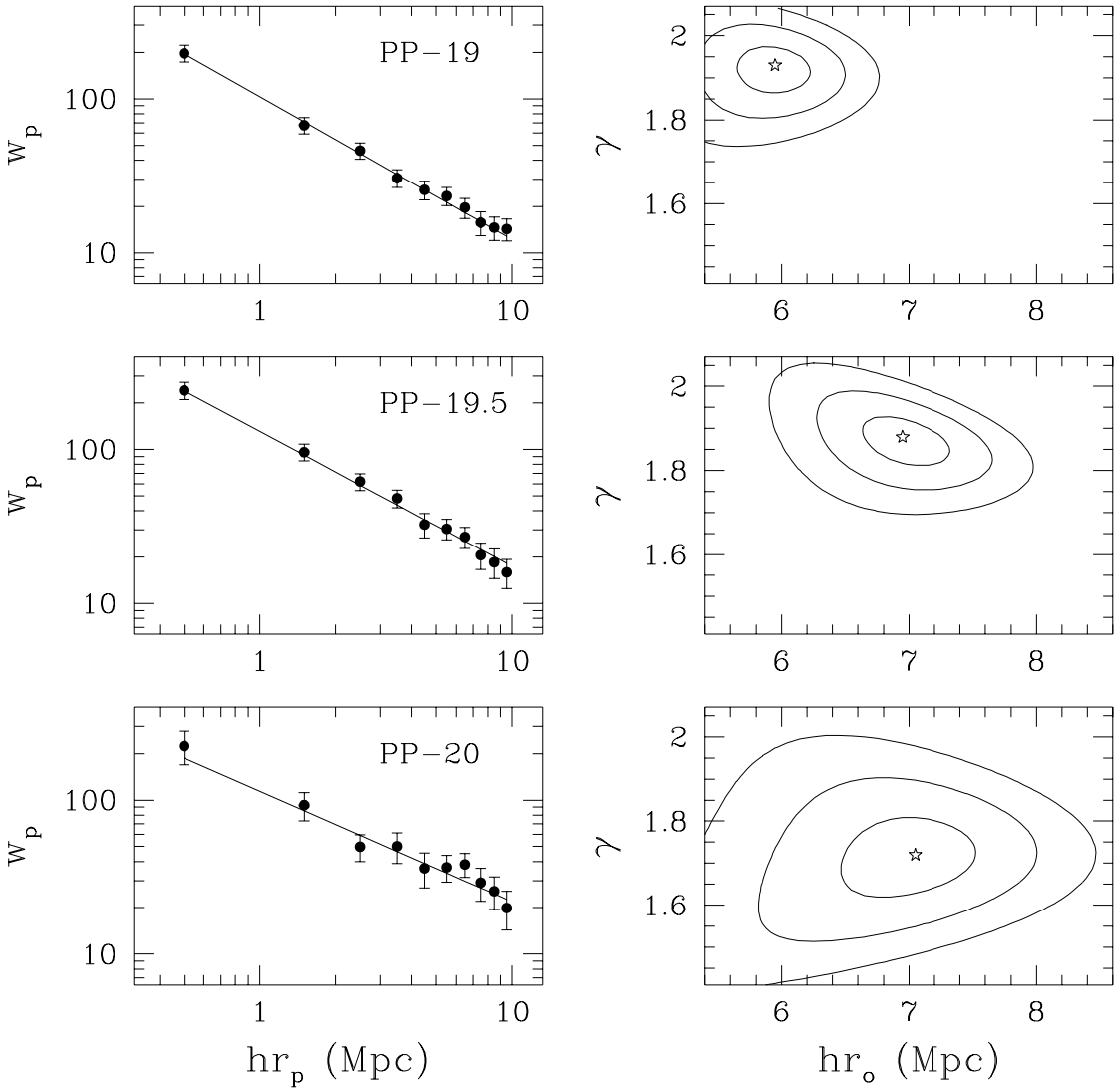

FIG. 8.—Projected correlation function $w_p(r_p)$ and results of fits of the power-law model for the three volume-limited samples. Error bars are given by bootstrap resampling. Contours give the 68.3%, 95.4%, and 99.73% confidence levels on the two parameters taken separately.

is most significant ($\sim 3\sigma$) between PP-19 and PP-19.5; r_0 does not grow significantly between PP-19.5 and PP-20. This is in qualitative agreement with the results of Iovino et al. (1993) using a previous version of this sample, and the results of Loveday et al. (1995) using the APM-Stromlo redshift survey, but it is in contrast to Hamilton (1988), who found that the luminosity dependence of r_0 was most significant at the highest luminosities. Table 2 also shows a similar trend for the spiral-only samples. Thus, even within morphological classes a luminosity dependence of clustering does exist (cf. Fig. 12 of Iovino et al. 1993).

TABLE 2

BEST-FIT PARAMETERS OF THE REAL-SPACE CORRELATION FUNCTION FROM $w_p(r_p)$

Sample	r_0 (h^{-1} Mpc)	γ
PP-19	$5.95^{+0.27}_{-0.31}$	$1.93^{+0.04}_{-0.07}$
PP-19.5	$6.95^{+0.37}_{-0.32}$	$1.88^{+0.05}_{-0.07}$
PP-19.5 (NP).....	$6.55^{+0.34}_{-0.36}$	$1.86^{+0.04}_{-0.05}$
PP-20	$7.05^{+0.47}_{-0.59}$	$1.72^{+0.09}_{-0.10}$
S-19	$4.55^{+0.36}_{-0.36}$	$1.65^{+0.06}_{-0.07}$
S-19.5	$5.55^{+0.40}_{-0.45}$	$1.73^{+0.07}_{-0.08}$
S-19.5 (NP).....	$5.05^{+0.54}_{-0.48}$	$1.76^{+0.08}_{-0.10}$
S-20	$5.05^{+0.61}_{-0.65}$	$1.85^{+0.08}_{-0.09}$
E-19.5	$8.35^{+0.75}_{-0.76}$	$2.05^{+0.10}_{-0.08}$

We have checked the sensitivity of these results to magnitude errors at the faint end by cutting the PP-19, PP-19.5, and PP-20 samples at a corrected magnitude $m_{Zw} = 15.2$, and recomputing $\xi(r_p, \pi)$, $w_p(r_p)$, and the best fit with a power-law $\xi(r)$. This is a fairly conservative selection, reducing each of the three subsamples by $\sim 30\%$ in number (to 882, 740, and 503 galaxies, respectively). For these three samples, we obtain estimates for (r_0, γ) of ($5.95^{+0.34}_{-0.30}$ h^{-1} Mpc, $1.92^{+0.06}_{-0.07}$), ($6.85^{+0.40}_{-0.41}$ h^{-1} Mpc, $1.90^{+0.11}_{-0.06}$), and ($7.45^{+0.64}_{-0.64}$ h^{-1} Mpc, $1.74^{+0.11}_{-0.10}$), respectively. Comparison of these values with those in Table 2 shows that the results are very robust and that our conclusions are unaffected by any magnitude bias affecting the faint end of the Zwicky catalogue.

Figure 9 shows one of our principal results, the relative clustering strength of early- and late-type galaxies as described by the real-space correlation function. Both the slope and correlation length are significantly different in the two samples (Table 2).

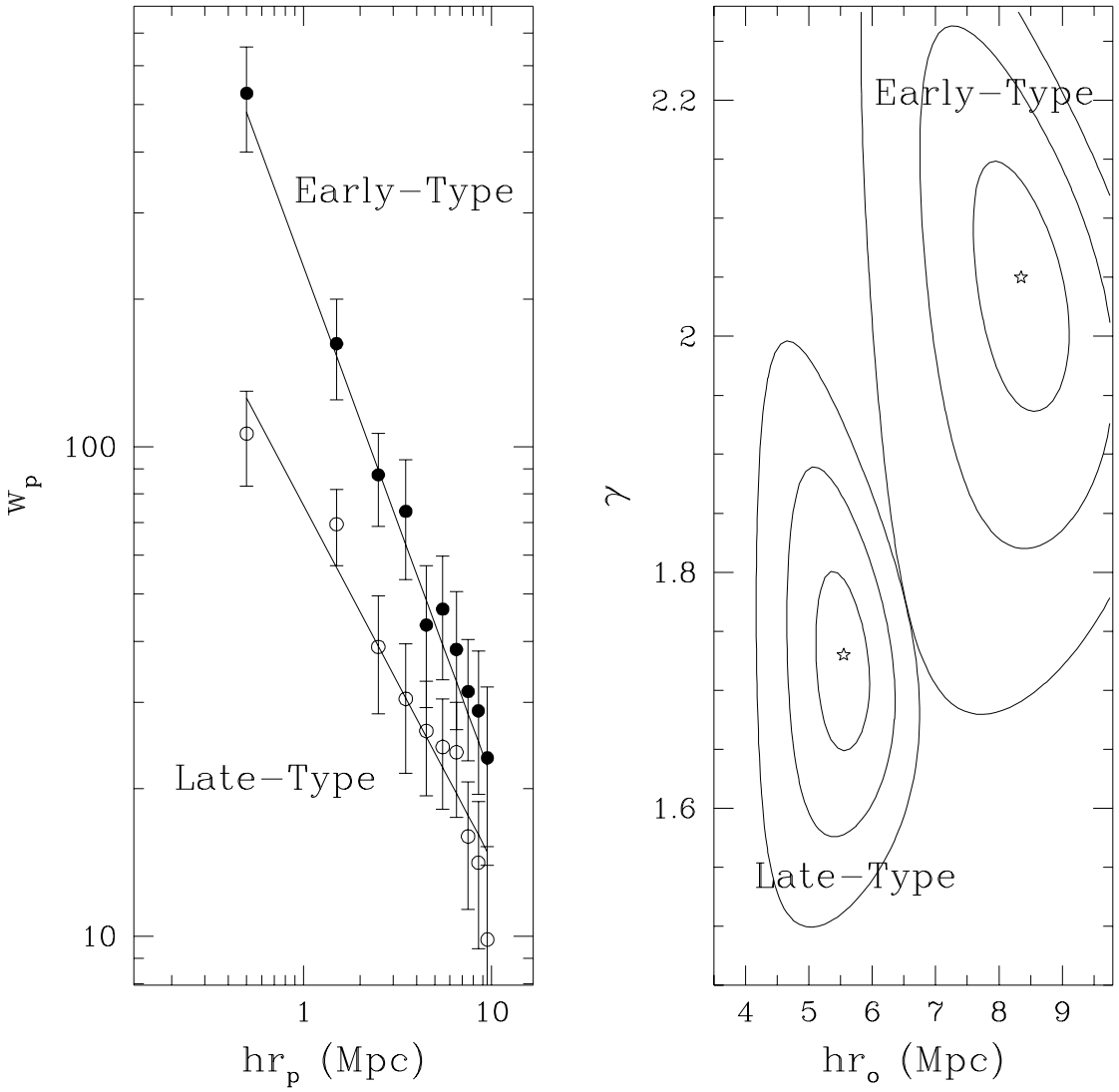

FIG. 9.—As Fig. 8, for early- and late-type galaxies separately. Note the very significant separation in parameter space between the two classes.

The scale dependence of the relative bias, b_{ES}, of early- to late-type galaxies is then simply

$$b_{ES}(r) = \left[\frac{\xi_E(r)}{\xi_S(r)}\right]^{1/2} = b_1 r^{-v}, \qquad (7)$$

where b_1 is the value at 1 h^{-1} Mpc and $v = (\gamma_S - \gamma_E)^{0.5}$. We find $b_{ES}(r) = (2.0 \pm 0.4)r^{-0.16\pm0.08}$, error bars computed using standard error propagation. At $r = 5$ h^{-1} Mpc, we find $b_{ES} = 1.6 \pm 0.4$. Hermit et al. (1996) compute a similar relative bias factor from the Optical Redshift Survey (Santiago et al. 1995), but in redshift space, finding an average value of ~ 1.5 between 1 and 10 h^{-1} Mpc. Their analysis does not take into account differences in redshift-space distortions between the two classes of galaxies that we have stressed here. Loveday et al. (1995) use both the APM catalogue and the sparsely sampled subsets of galaxies that form the APM-Stromlo redshift survey; inverting the angular correlation function $w(\theta)$ for two subsamples limited to $b_J = 16.57$, they find $r_0 = 7.76 \pm 0.35$ h^{-1} Mpc, $\gamma = 1.87 \pm 0.07$ for early-type galaxies and $r_0 = 4.49 \pm 0.13$ h^{-1} Mpc, $\gamma = 1.72 \pm 0.05$ for late-type galaxies. This is in good agreement with our direct estimates from the spatial function. However, the APM-Stromlo data are too sparse to be able to compute $\xi(r_p, \pi)$ directly from the morphological subsamples, so that an estimate of the pairwise velocity dispersion $\sigma_{12}(r)$ cannot be obtained.

The correlation length we find for all spiral galaxies is significantly larger than found for *IRAS* galaxies in the 1.2 Jy redshift survey, $r_0(1.2\text{ Jy}) = 3.76^{+0.20}_{-0.23}$ h^{-1} Mpc, while the slope, $\gamma(1.2\text{ Jy}) = 1.66^{+0.12}_{-0.09}$, is similar. This has the interesting implication that the relative bias of spiral galaxies to *IRAS*-selected galaxies is independent of scale, at least below 10 h^{-1} Mpc. Since *IRAS* galaxies tend to be of type Sb and later, we have defined a volume-limited sample to $M = -19$, containing 321 galaxies with types between Sb and Irr. In fact, for these we find a lower correlation length, $r_0 = 4.05^{+0.57}_{-0.75}$ h^{-1} Mpc, and a similar logarithmic slope, $\gamma = 1.55^{+0.11}_{-0.13}$, in excellent agreement with *IRAS* galaxies.

4.3. *The Pairwise Velocity Dispersion*

The quantity $\xi(r_p, \pi)$ can be expressed as an integral over the product of the real-space correlation function, $\xi(r)$, and the distribution function of the line-of-sight components, w_3, of relative velocities for pairs with separation $r, f(w_3 | r)$ (F94b). If y is the component of r along the line of sight, then $w_3 = H_0(\pi - y)$, and the integral can be written as (Peebles

1980; F94b)

$$1 + \xi(r_p, \pi) = H_0 \int_{-\infty}^{+\infty} dy \times \{1 + \xi[(r_p^2 + y^2)^{1/2}]\} f[H_0(\pi - y) | r] . \quad (8)$$

This expression gives a *description* of the effect of a peculiar velocity field on $\xi(r)$, but does not represent a self-consistent dynamical treatment of the density and velocity fields, which are clearly interdependent (Fisher 1995). We do not have any a priori information, therefore, on the functional form of the distribution function f. Peebles (1976) first showed that an exponential distribution best fits the observed data, a result subsequently confirmed by N-body models (e.g., Zurek et al. 1994). With such a choice, equation (8) becomes

$$1 + \xi(r_p, \pi) = H_0 \int_{-\infty}^{+\infty} dy[1 + \xi(r)] \frac{1}{\sqrt{2}\sigma_{12}(r)} \times \exp\left\{ -\sqrt{2} H_0 \left| \frac{\pi - y[1 + v_{12}(r)/H_0 r]}{\sigma_{12}(r)} \right| \right\}, \quad (9)$$

where $r^2 = r_p^2 + y^2$, $v_{12}(r)$ is the mean relative velocity of galaxy pairs with separation r, and $\sigma_{12}(r)$ is the pairwise one-dimensional velocity dispersion along the line of sight.

F94b show that it is very difficult to model the dependence of v_{12} on the separation r. This is particularly difficult in our case, as our sample covers too small a volume to allow a determination of the large-scale streaming from the compression of the contours of $\xi(r_p, \pi)$ (see § 4.1). For this reason, we do not follow F94b in a detailed analysis of the mean streaming; instead, we limit ourselves to the simple streaming model introduced by DP83, based on the similarity solution of the BBGKY equations,

$$v_{12}(r) = -H_0 r \frac{F}{1 + (r/r_0)^2} . \quad (10)$$

We wish to fit equation (9) to the observed $\xi(r_p, \pi)$ in order to constrain $\sigma_{12}(r)$. We are particularly interested in $\sigma_{12}(1)$, the pairwise velocity dispersion for scales smaller than 1 h^{-1} Mpc, and thus we carry out all fits to the quantity

$$\xi(\pi) = \int_0^1 dr_p \, \xi(r_p, \pi) , \quad (11)$$

following F94b.[9] In practice, because we have calculated $\xi(r_p, \pi)$ in 1 h^{-1} Mpc bins, $\xi(\pi)$ is simply the value of $\xi(r_p, \pi)$ in the first bin of r_p. We assume further that $\sigma_{12}(r)$ is a weak function of separation r (DP83), so that it can be treated as a single free parameter, $\sigma_{12}(1)$. Figure 10 shows the results of two-parameter fits of the model of equations (9) and (10) to $\xi(\pi)$ for the E-19.5 and S-19.5 subsamples. We use the best-fit values of r_0 and γ from Table 2 appropriate to each subsample; errors and covariances of $\xi(\pi)$ are calculated consistently, as described in § 3.3. The quantity F is very poorly constrained by these data (Fig. 10), as the free-streaming on these small scales is quite small.

We therefore estimate $\sigma_{12}(1)$ for the two cases $F = 0$ (free expansion of pairs with the Hubble flow) and $F = 1$ (stable clustering). The second of these is probably closer to a realistic model; Jain (1997) shows that the stable clustering hypothesis ($F = 1$) should be a good approximation at the present epoch for scales of the order of, or smaller than, 0.7 h^{-1} Mpc. We thus use values $F = 1$ in our discussion below.

The value of $\sigma_{12}(1)$ is of the order of 800 km s^{-1} for PP-19 and PP-19.5, but drops below 500 km s^{-1} for PP-20, consistent with the more isotropic contours of $\xi(r_p, \pi)$ for this case (Fig. 6). We interpret this as due to the smaller effect that rich clusters, and in particular the Perseus cluster, have on the larger volume of PP-20, as we show in the next section. Notice the very significant factor of 2 difference between the $\sigma_{12}(1)$ for early- and late-type galaxies at $M_{Zw} = -19.5$, a dramatic indication of the effect of cluster cores on the determination of $\sigma_{12}(1)$. We now turn to a direct demonstration of the sensitivity of $\sigma_{12}(1)$ to the presence of rich clusters in the sample.

4.4. *Stability of σ_{12} for Late-Type Galaxies*

Marzke et al. (1995) have discussed in detail the effect of the contribution of cluster galaxies to the small-scale pairwise velocity dispersion. The pairwise velocity dispersion is a pair-weighted statistic, and thus is heavily weighted in regions of high density, i.e., clusters. Because galaxies in clusters have an intrinsically high velocity dispersion, the inclusion or exclusion of clusters can have a dramatic effect on σ_{12}. Marzke et al. (1995) showed that estimates of $\sigma_{12}(r)$ fluctuate from one sample to another when there are significant variations in the number of clusters even over volumes as large as those of the CfA2 and SSRS2 surveys. Guzzo et al. (1996) showed that $\sigma_{12}(1)$ dropped from $\sim$800 km s^{-1} to $\sim$600 km s^{-1} in PP-19 after removing the Perseus cluster. Thus, the removal of a single dominant cluster can significantly affect the pairwise velocity dispersion.

Here we further explore the stability of $\sigma_{12}(1)$ in the case of spiral galaxies. Using spiral-only samples, we are in practice filtering out the high-density nonlinear regions that would otherwise get such high weight in $\sigma_{12}(1)$. The result of excluding the Perseus cluster from the PP-19.5 sample is visually shown by the changes in $\xi(r_p, \pi)$ in the two top panels of Figure 11. The differences between the contours in the two panels [and the corresponding values of $\sigma_{12}(1)$ reported in Table 3] can be compared to those produced by the same operation on the S-19.5 sample (*bottom*). While the

TABLE 3

BEST ESTIMATES OF PAIRWISE VELOCITY DISPERSION

Sample	$\sigma_{12}(1)$ ($F = 0$)	$\sigma_{12}(1)$ ($F = 1$)
PP-19	775^{+85}_{-65}	855^{+85}_{-75}
PP-19.5	735^{+155}_{-115}	805^{+155}_{-115}
PP-19.5 (NP).....	625^{+125}_{-85}	725^{+135}_{-95}
PP-20	525^{+155}_{-115}	465^{+145}_{-105}
S-19	205^{+75}_{-55}	295^{+75}_{-55}
S-19.5	255^{+95}_{-65}	345^{+95}_{-65}
S-19.5 (NP).....	235^{+115}_{-75}	325^{+125}_{-85}
S-20	415^{+465}_{-245}	485^{+465}_{-245}
E-19.5.....	815^{+245}_{-165}	865^{+250}_{-165}

NOTE.—Summary of the best estimates of the pairwise velocity dispersion between 0 and 1 h^{-1} Mpc, $\sigma_{12}(1)$, for the two cases $F = 0$ (free streaming with the Hubble flow) and $F = 1$ (stable clustering). All estimates are in km s^{-1}.

[9] Our definition of $\xi(\pi)$ differs from that of F94b by an unimportant normalization factor; cf. their eq. (7).

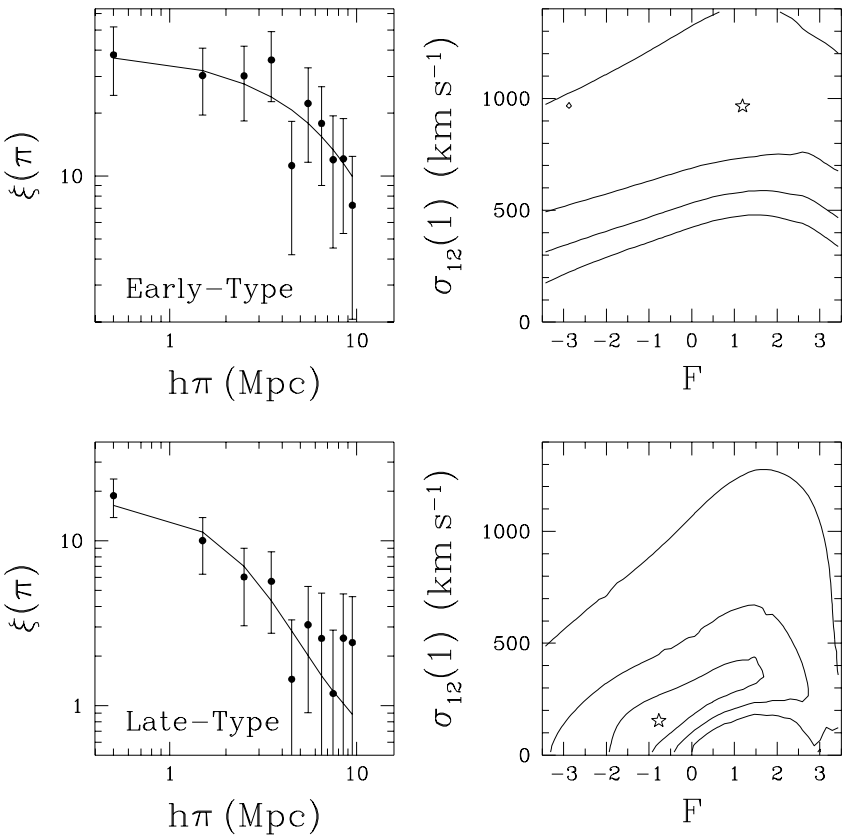

FIG. 10.—Example of full two-parameter fits to $\xi(r_p, \pi)$ based on the model of eq. (9), to show how poorly constrained the streaming amplitude F is. Contour levels are as in Fig. 8.

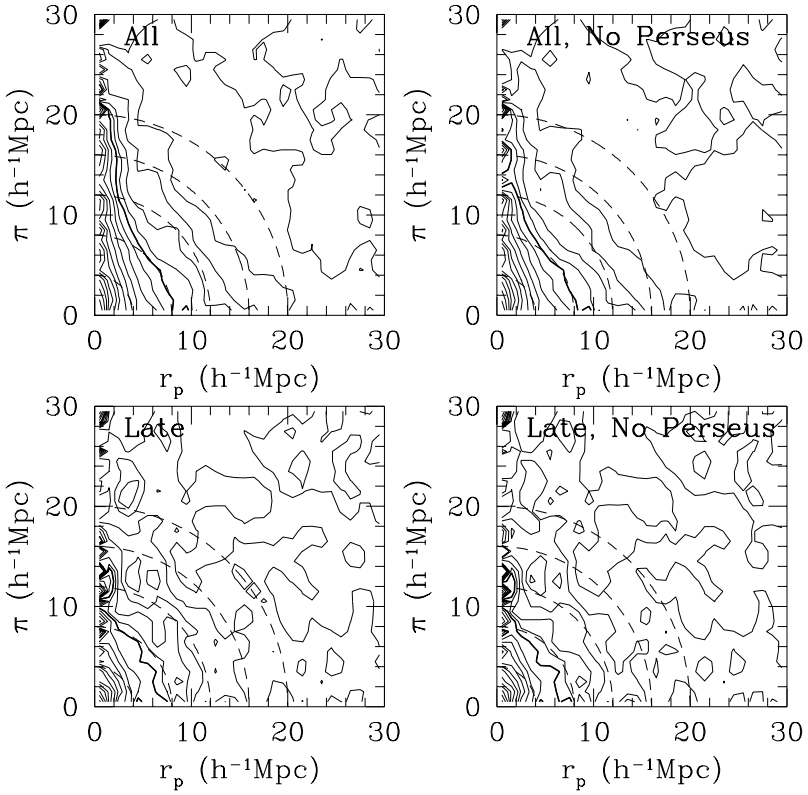

FIG. 11.—Effect on $\xi(r_p, \pi)$ of removing the largest "finger of God" from the sample. Right panels show the effect of excluding the high velocity dispersion Perseus cluster. Top panels are for PP-19.5, bottom for S-19.5. Note the change between the two top panels, while for spirals the removal of the cluster has very little effect on the measured $\xi(r_p, \pi)$.

effect on PP-19.5 is relevant (although less dramatic than was found for PP-19 by Guzzo et al. 1996, owing to the larger volume and the consequent reduced weight of the Perseus cluster), the two bottom panels of Figure 11 are virtually identical, and so are the estimated values of $\sigma_{12}(1)$.

Table 3 also gives $\sigma_{12}(1)$ for spiral samples limited to $M_{Zw} = -19$ and -20. Table 3 indicates that $\sigma_{12}(1)$ for spirals lies consistently between 300 and 350 km s^{-1}. This agrees with the F94b value for *IRAS* galaxies, 317^{+40}_{-49} km s^{-1}, the Marzke et al. (1995) value for galaxies outside of $R \geq 1$ Abell clusters, 295 ± 99 km s^{-1}, and the original determination by DP83, which undersampled the Virgo cluster in CfA1 (Somerville et al. 1997).

It is interesting to discuss the similarity of $\sigma_{12}(1)$ for spiral and *IRAS* galaxies in light of their different correlation lengths ($r_0 \simeq 5.5\ h^{-1}$ Mpc and $r_0 \simeq 3.8\ h^{-1}$ Mpc, respectively). *IRAS* galaxies are mostly late-type spirals, and indeed we have shown above that if we compute $\xi(r)$ for this subclass, we recover $r_0 \simeq 4.0\ h^{-1}$ Mpc, in agreement with *IRAS* galaxies (cf. Giovanelli et al. 1986 and Iovino et al. 1993, who showed that there is a continuity in the clustering strength within the spiral class, with Sc's being less clustered than Sa's). The similar values of $\sigma_{12}(1)$, on the other hand, may simply indicate that the dynamics of *IRAS* galaxies and all spirals are governed by the same fluctuations in the underlying matter density field. Indeed, $\sigma_{12}(1)$ for galaxies of type Sb and later is found to be 255^{+105}_{-75} km s^{-1}, in statistical agreement with the spiral sample as a whole.

5. SUMMARY AND DISCUSSION

The main conclusions we have reached in this paper can be summarized as follows.

1. We see very strong small-scale redshift-space distortions in the Perseus-Pisces redshift survey. The distortions are much stronger for early-type galaxies, as one would expect from the segregation of morphological types.

2. We confirm a mild luminosity dependence of clustering for absolute magnitudes around the knee of the luminosity function, $M_{Zw} \sim -19.5$; the correlation length increases from $5.95^{+0.27}_{-0.31}\ h^{-1}$ Mpc for $M_{Zw} \leq -19$ to $7.05^{+0.47}_{-0.59}\ h^{-1}$ Mpc for $M \leq -20$. These values are somewhat higher than the "canonical" value of the correlation length based on the DP83 analysis of the CfA1 survey, $r_0 = 5.4\ h^{-1}$ Mpc. This latter value is confirmed by the analysis of the ESO Slice Project (ESP) survey (Bartlett et al. 1997), yielding $r_0 = 4.5^{+0.15}_{-0.17}\ h^{-1}$ Mpc; the Las Campanas survey (Lin 1995) gives $r_0 = 5.00 \pm 0.14\ h^{-1}$ Mpc. There are probably two reasons for the higher values of r_0 measured here. First, the "standard" values quoted above are estimates of $\xi(r)$ performed on apparent-magnitude–limited samples. If there is, as we have seen, a mild luminosity dependence on clustering, samples that are volume-limited at relatively bright absolute magnitudes will systematically measure a higher clustering signal. Second, the Perseus-Pisces area is rather rich in clusters of galaxies, so that it probably overemphasizes the cluster contribution to $\xi(r)$. For comparison, the richest cluster in the CfA1 volume is the Virgo cluster. The CfA2 + SSRS2 sample (Marzke et al. 1995) covers part of the PP area and thus has a higher contribution of clusters, resulting in $r_0 = 5.97 \pm 0.15\ h^{-1}$ Mpc.

3. A meaningful comparison of the relative clustering strength of spirals and ellipticals can be performed only in real space, i.e., after correcting for the effect of differential redshift-space distortions. A power-law shape, $\xi(r) = (r/r_0)^{-\gamma}$, is a good representation of the real-space correlation function between 1 and 10 h^{-1} Mpc for both ellipticals and spirals. Our best-fit estimate of the power-law parameters gives $r_0 = 8.35^{+0.75}_{-0.76}\ h^{-1}$ Mpc, $\gamma = 2.05^{+0.10}_{-0.08}$ for ellipticals, and $r_0 = 5.55^{+0.40}_{-0.45}\ h^{-1}$ Mpc, $\gamma = 1.73^{+0.07}_{-0.08}$ for spirals. We model the relative bias of the two types of galaxies as a power law with a mild dependence on scale, $b_{ES}(r) = (2.0 \pm 0.4)(r/1\ h^{-1}\ \text{Mpc})^{-0.16 \pm 0.08}$. Furthermore, we confirm the continuous variation of clustering strength within the spiral class. For late-type spirals (Sb and later) and irregulars, we estimate $r_0 = 4.05^{+0.57}_{-0.75}\ h^{-1}$ Mpc and $\gamma = 1.55^{+0.11}_{-0.13}$, virtually the same correlation function as *IRAS* galaxies.

4. The quantity $\sigma_{12}(1)$, the measured pairwise velocity dispersion between 0 and 1 h^{-1} Mpc, varies considerably between samples of different volumes, ranging from 855^{+85}_{-75} km s^{-1} for PP-19 to 465^{+145}_{-105} km s^{-1} for PP-20. This variation is consistent with the smallness of the volume sampled.

5. The difference in the measured $\sigma_{12}(1)$ between early- and late-type galaxies is remarkable. We estimate $\sigma_{12}(1) = 865^{+250}_{-165}$ km s^{-1} for ellipticals and $\sigma_{12}(1) = 345^{+95}_{-65}$ km s^{-1} for spirals. Contrary to results for the combined sample, the value of $\sigma_{12}(1)$ for spiral galaxies alone is stable to both changes in the sample volume and the presence of rich clusters. The consistency of this value with those measured for noncluster galaxies (Marzke et al. 1995) and *IRAS* galaxies (F94b) and its stability among spiral subclasses (for Sb and later types we measure 255^{+105}_{-75} km s^{-1}) suggest that a value $\sigma_{12}(1)$ in the range 300–350 km s^{-1} is a good estimate of the "temperature" of the galaxy flow outside of virialized structures.

L. G. gratefully thanks J. P. Ostriker for hospitality at Princeton University, where part of this work was done, and J. Bartlett, M. Davis and P. J. E. Peebles for fruitful discussions. We thank the referee, Ron Marzke, for his valuable comments and suggestions. M. A. S. acknowledges the generous support of the Alfred P. Sloan Foundation. This work was partly supported by grants AST 90-23450 and AST 95-28860 to M. P. H. and AST 94-20505 to R. G.

REFERENCES

Bartlett, J. G., et al. 1997, A&A, submitted
Bothun, G. D., & Cornell, M. E. 1990, AJ, 99, 1004
Burstein, D., & Heiles, C. 1978, ApJ, 225, 40
Davis, M., & Geller, M. J. 1976, ApJ, 208, 13
Davis M., & Peebles, P. J. E. 1983, ApJ, 267, 465 (DP83)
Dressler, A. 1980, ApJ, 236, 351
Eisenstein, D. J., Loeb, A., & Turner, E. L. 1997, ApJ, 475, 421
Fisher, K. B. 1995, ApJ, 448, 494
Fisher, K. B., Davis, M., Strauss, M. A., Yahil, A., & Huchra, J. P. 1994a, MNRAS, 266, 50 (F94a)
———. 1994b, MNRAS, 267, 927 (F94b)
Giovanelli, R., & Haynes, M. P. 1991, ARA&A, 29, 499
Giovanelli, R., Haynes, M. P., & Chincarini, G. L. 1986, ApJ, 300, 77
Giovanelli, R., Haynes, M. P., Wegner, G., da Costa, L., Freudling, W., & Salzer, J. 1996, ApJ, 464, L99
Guzzo, L., Fisher, K. B., Strauss, M. A., Giovanelli, R., & Haynes, M. P. 1996, Astrophys. Lett. Commun., 33, 231
Hamilton, A. J. S. 1988, ApJ, 332, 67
———. 1993, ApJ, 417, 19
Hermit, S., Lahav, O., Santiago, B. X., Strauss, M. A., Davis, M., Dressler, A., & Huchra, J. P. 1996, MNRAS, 283, 709
Huchra, J. P., Davis, M., Latham, D., & Tonry, J. 1983, ApJS, 52, 89

Iovino, A., Giovanelli, R., Haynes, M. P., Chincarini, G., & Guzzo, L. 1993, MNRAS, 265, 21
Iovino, A., Warren, S. J., Shaver, P. A., & Hewett, P. 1996, Astrophys. Lett. Commun., 33, 143
Jain, B. 1997, MNRAS, 287, 687
Lin, H. 1995, Ph.D. thesis, Harvard Univ.
Ling, E. N., Frenk, C. S., & Barrow, J. D. 1986, MNRAS, 223, 21P
Loveday, J., Maddox, S. J., Efstathiou, G., & Peterson, B. A. 1995, ApJ, 442, 457
Marzke, R. O., Geller, M. J., da Costa, L. N., & Huchra, J. P. 1995, AJ, 110, 477
Mo, H. J., Jing, Y. P., & Börner, G. 1993, MNRAS, 264, 82
Peebles, P. J. E. 1976, Ap&SS, 45, 3
Peebles, P. J. E. 1980, The Large-Scale Structure of the Universe (Princeton: Princeton Univ. Press)
Postman, M., & Geller, M. J. 1984, ApJ, 281, 95
Santiago, B. X., Strauss, M. A., Lahav, O., Davis, M., Dressler, A., & Huchra, J. P. 1995, ApJ, 446, 457
Somerville, R. S., Davis, M., & Primack, J. R. 1997, ApJ, 479, 616
Strauss, M. A., Davis, M., Yahil, A., & Huchra, J. P. 1992, ApJ, 385, 421
Willick, J. A. 1990, ApJ, 351, L5
Zurek, W., Quinn, P. J., Warren, M. S., & Salmon, J. K. 1994, ApJ, 431, 559
Zwicky, F., Herzog, E., Wild, P., Karpowicz, M., & Kowal, C. 1961-1968, Catalogue of Galaxies and of Clusters of Galaxies (Pasadena: California Inst. Technology)